Interdecadal Change in the Effect of Tibetan Plateau Snow Cover on Spring Precipitation over Eastern China around the Early 1990s

Chao Zhang
  Institute of Atmospheric Sciences, Fudan University
Yuanyuan Guo
  Department of Atmospheric and Oceanic Sciences and Institute of Atmospheric Sciences, Fudan University
Zhiping Wen (✉ zpwen@Fudan.edu.cn)
  Fudan University   https://orcid.org/0000-0003-1259-0362

Research Article

Abstract

Previous works extensively investigated the influences of the winter-spring Tibetan Plateau snow cover (TP, TPSC) on climate variability over the East Asia. The present work documents an interdecadal-changed impacts of different spring TPSC anomaly (TPSCA) patterns on spring precipitation over eastern China (SPEC) around the early 1990s. It is found that the correlation of eastern and western TPSCA shifts from negative to positive around 1990. The empirical orthogonal function (EOF) analysis applying onto the spring TPSCA during 1970−1989 (P1) and during 1991−2017 (P2) adds additional support for such interdecadal change in the relationship between the eastern and western TPSCA. Specifically, the leading EOF (EOF1) mode in P1 shows an out-of-phase pattern with opposite signals lying over the eastern and western TP, while the counterpart in P2 is characterized by an in-phase pattern over the entire TP. Corresponding to more (less) snow cover in the eastern (western) TP in P1, a significant TP cold cyclone (TPCC) and a downstream anticyclone over the western North Pacific are observed. Anomalous southerly flow prevailing east to TPCC could bring the warm-wet air from tropics to the coast of East Asian, which largely enhances the spring precipitation south to Yangtze River Valley (YRV). By contrast, regarding more snow cover both in the eastern and western TP in P2, a relatively northward-displaced and wider TPCC sweeps over the entire TP compared with the TPSC-induced TPCC in P1. Moreover, there are significant sinking anomalies observed in the downstream YRV-HRV region, which leads to suppressed spring precipitation over there via the dry-cold advection process. Hence, these discrepancies of local and downstream atmospheric circulation induced by the out-of-phase and in-phase TPSCA patterns in two epochs play an important role in resulting in the interdecadal shift of the SPEC anomaly pattern around 1990.

1. Introduction

TP snow can exert profound impacts on local energy budgets and hydrological processes owing to its specific high elevation, emissivity, reflectivity and low thermal conductivity (Dickson 1984; Yasunari et al. 1991; Xiao and Duan 2016; Wang et al. 2019). Moreover, the remote effect of anomalous TP snow has also been emphasized on the downstream even global climate systems (Xu et al. 2012; Fan et al. 2014; Li et al. 2018; Wang et al. 2018, 2020) by modulating the snow-albedo, snow-hydrology, and snow-diabatic heating physical processes (Hahn and Shukla 1976; Barnett et al. 1988a;1999b; Lin and Wu 2011a, 2012b; Zhang et al. 2021).

The current literature which examined the impacts of preceding Tibetan Plateau snow cover (TPSC) anomaly (TPSCA) on ensuring downstream climate systems have highlighted the remarkable discrepancies of TPSCA located over the eastern and western TP, respectively. In detail, one of their discrepancies exists in the variation of snow itself over the western and eastern TP (Xiao and Duan 2016; Wang et at. 2018, 2019; Jia et al. 2021; Han et al. 2021). For instance, Xiao and Duan (2016) revealed that snow cover along the Himalayas (i.e., western TP) can prolong the signature of snow cover anomaly from winter to summer, whereas the eastern TPSCA in winter can only persist till the early spring. These discrepancies lying in the eastern and western TP snow itself, in turn, lead to the distinct climate effects

(Zhang et al. 2004; Si and Ding 2013; Fan et al. 2014; Liu et al. 2014; Xiao and Duan 2016). Si and Ding (2013) found that the heavier winter snow over the eastern TP, more often than not, favors a northward replacement of the East Asian summer precipitation. Xiao and Duan (2016) argued that the excessive May TPSC over the western TP inclines to a wetter summer over the YRV-HRV. As already referred, the different responses of atmospheric circulation to the eastern or western TPSCA have been relatively clearly proposed by previous studies. Nevertheless, the combined effect of the western and eastern TPSC still remains uncertain. A better understanding of this issue will be extremely conductive to improve the accuracy of downstream climate prediction.

The impacts of TPSCA on spring-summer precipitation over eastern China have been extensively investigated (e.g., Si and Ding 2013; Xiao and Duan 2016; Wang et at. 2018; Zhang et al. 2021). Due to summer as the main rainfall season over eastern China, a chain of studies investigated the influence of TPSCA on the summer precipitation over eastern China. However, the amplitude of spring precipitation over eastern China (SPEC) almost equals to that of the summer rainfall (Cheng et al. 2018; You and Jia 2018; Xu et al. 2019), whereas the SPEC features striking variability at multiple time scales (Yang and Lau 2004; Feng and Li 2011; Zhu et al. 2014). In essence, the preceding TPSCA may also be one of the potential factors of SPEC (e.g., Jia et al. 2021). Jia et al (2021) revealed that the preceding TPSC can impact the SPEC by modulating the subsequent upper-level East Asian subtropical westerly jet and lower-troposphere southerly. However, due to the atmospheric chaotic nature, the atmospheric signals cannot be prolonged for more than half a month (Qian et al. 2019). The simultaneous spring TPSC may exert a direct impact on the SPEC, thereby exploring the simultaneous connection between TPSC and SPEC will aid to a better acquaintance with the physical processes of the variability of SPEC. In addition, both TP snow and SPEC have been undergone the pronounced interdecadal changes in the 1990s (Zhang et al. 2004; Wu et al. 2012a, 2012b; Si and Ding 2013; Fan et al. 2014; Qian et al. 2019; Xu et al. 2019; Zhang et al. 2021). However, it is by no means certain whether the interdecadal change lies in the climate effect of TPSC on SPEC, which calls for a need to further examine whether and how the TPSC affects the SPEC around the early 1990s. Note that previous evidences having been demonstrated that the El Niño-Southern Oscillation (ENSO) related tropical Pacific sea surface temperature anomaly (SSTA) is one of the key determinants of the SPEC (Yang and Lau 2004; Li et al. 2018; Jia et al. 2019). Hence, when we consider the relationship of TPSC and SPEC, the ENSO signals has been removed in the present study.

The above questions will be explored in the current study through the observational data, and the findings will be further verified via model experiments. Following the above introduction in section 1. The data, methodology, and model in the present work will be introduced in section 2. Section 3 investigates the interdecadal change in the relationship of the eastern and western TPSC and its linkage with the spring precipitation. Possible mechanisms responsible for the effect of TPSC on the spring precipitation will be delved in section 4, followed by the conclusions and discussions in last section.

2. Data, Methods, And Model

a. Data

The monthly Northern Hemisphere snow cover dataset at a horizontal resolution of 2°×2° grid used here is available from the National Oceanic and Atmospheric Administration (NOAA) Climate Data Record of the Northern Hemisphere (Robinson et al. 2012). The monthly snow cover data is converted from the original weekly production that is high-resolution radiometers-based and multiple satellites-based snow cover data (Brodzik and Armstrong 2013), with a horizontal resolution of 25 km and spanning 1967 to the present, which is derived from the National Snow and Ice Data Center (available at http://nsidc.org/data/).

Monthly mean precipitation data covering 1970−2017 in the current study has been converted into a spatial resolution of 1° in longitude by 1° in latitude based on the daily 741 gauge-stations with good consecutive measurements spanning main land China, which are collected from the China Meteorological Administration (http://data.cma.cn/en/?r=data/index&cid=6d1b5efbdcbf9a58).

Monthly mean and daily mean atmospheric variables are derived from the National Centers for Environmental Prediction reanalysis during 1948-present (Kalnay et al. 1996; http://www.esrl.noaa.gov/psd/). The datasets, with a spatial resolution 2.5°×2.5° grid, comprise air temperature, omega, specific humidity, precipitation rate, wind and surface pressure containing 17 vertical pressure levels.

Monthly mean sea surface temperature, with a spatial resolution of 1° in longitude by 1° in latitude for 1870-present, is collected from the Met Office Hadley Center (Rayner et al. 2003; https://www.metoffice.gov.uk/hadobs/hadisst/).

To exclude the influence of ENSO, the boreal winter-spring Niño 3.4 index is used in this study to reflect its variability, which is retrieved from the Earth System Research Laboratory of NOAA (https://www.esrl.noaa.gov/psd/data/climateindices/list).

b. Methods

Due to focus on the interannual time scale, all variables are operated by detrending linear trend and high pass filter with signals less than 8 year retained to attain the interannual component of variables. Other statistical tools, including partial regression by removing the ENSO signals to investigate whether the TPSC-SPEC relationship is independent of ENSO, linear regression analysis and Student t test, are also adopted in this work. Eastern China (20−38°N, 100−122°E) to be covered with south to YRV (20−29°N, 100−120°E) and the YRV-HRV (29−38°N, 100−122°E), is our interested domain to examine the spring precipitation variation.

The atmospheric apparent heat source (Q_1) in the atmospheric column is calculated to reflect the TPSCA-induced thermal effect on the overlying air. Following Yanai et al (1973), Q_1 at each level in Eq. (1) and tropospheric integrated in Eq. (2) are given as follows:

$$Q1 = C_p \cdot \left[\frac{\partial T}{\partial t} + V \cdot \nabla_p T + \left(\frac{P}{P_0} \right)^k \cdot \omega \frac{\partial \theta}{\partial P} \right], \tag{1}$$

$$\langle Q1 \rangle = \frac{1}{g} \int_{Pt}^{Ps} Q1 dP. \tag{2}$$

where $k = R/C_p$, C_p and R refer to specific heat at constant pressure of dry air and gas constant, respectively. T, V, ω and θ are air temperature, horizontal wind, vertical velocity and potential temperature, respectively. Here, the diabatic heating over the TP is vertically integrated from surface (Ps) to 300hPa (Pt).

c. Model

The linear baroclinic model (LBM) utilized in the current work was provided by Watanabe and Kimoto (2000) and has been used for various purposes. According to the dynamical core of the Atmospheric General Circulation Model (AGCM), the LBM is elaborately designed by the Center for Climate System Research, University of Tokyo, and the National Institute for Environmental Studies, Japan. By imposing climatological spring mean flow and the idealized forcing associated with observational anomalies in a specific area, e.g., anomalous TP cooling/heating, the numerical model can reproduce the linear atmospheric response via time integration method. The model response can further provide insights into the mechanisms responsible for the effect of TPSCA-induced-cooling on the atmospheric circulation. Here, we employed the dry version with 20 vertical sigma levels and a horizontal T42 resolution.

Table 1 The details in the TP forcing model experiments

Basic state	Forcing	Extremum (K/day)	Radius (Lon × Lat)	Central location
P1	western TP heating (EXP1)	+1.6	6.0° × 6.0°	74.0°E, 36.0°N
	southeastern TP cooling (EXP2)	-1.9	4.5° × 2.5°	94.5°E, 30.5°N
P2	mid-western TP cooling (EXP3)	-2.0	4.5° × 4.0°	84.0°E, 33.5°N
	eastern TP cooling (EXP4)	-2.2	5.0° × 4.5°	96.5°E, 31.0°N
P2	southeastern TP cooling_P2 (EXP5)	-1.9	4.5° × 2.5°	94.5°E, 30.5°N
P1	eastern TP cooling_P1 (EXP6)	-2.2	5.0° × 4.5°	96.5°E, 31.0°N

3. Interdecadal Change In The Relationship Of The Eastern And Western Tpsca And Its Linkage With The Spring Precipitation

a. Interdecadal change in the relationship of the eastern and western TPSC

The climatological TPSC in spring, taken as the mean of March-April-May, together with its interannual standard deviation are displayed in Figure 1a. Both spring climatological snow cover and standard deviation are featured by two prominent centers over the western TP and eastern TP. Upon examination of the relationship between western and eastern TPSCA via constructing two interannual snow cover indices by taking their area-weighted average of snow cover over the western and eastern TP, respectively (Fig. 1b), we note that the relationship of these two snow cover indices exhibit a striking change from an out-of-phase variation to an in-phase variation around 1990. The temporal correlation coefficients (TCCs) with a 17-years sliding window, applied onto the western and eastern TP snow cover indices, add support to such interdecadal change in the western-eastern TPSCA relationship due to an abrupt increasing of TCCs from negative correlation before 1990 to positive after 1991 (Fig. 1c). Furthermore, such interdecadal shift is insensitive to the sliding window by changing it from 13-years to 19-years (figure not shown).

According to these results, the studying period was divided into two epochs, that is, 1970–1989 (referred as P1) and 1991–2017 (referred as P2). We reconstructed a TPSC indices (TPSCI) to measure the out-of-phase and in-phase relationship of the western and eastern TPSC indices during the periods of P1 and P2, respectively. The TPSCI in P1 is normalized by the difference of snow cover anomalies averaging over the eastern and western TPSC, and the counterpart in P2 is determined by the normalized summation of snow cover anomalies averaging over the eastern and western TPSC.

To examine whether the TPSCI could illustrate such interdecadal shift reasonably, the TPSCI was compared with the empirical orthogonal function (EOF) results obtained from the interannual component of spring TPSCA for both epochs, shown in Fig. 2. The leading EOF mode accounts for 20.0% and 22.1% of the total variance in P1 and P2, respectively. The spatial structure of EOF1 shifts from a western-eastern dipole pattern in P1 (Fig. 2a) to a monopole type in P2 (Fig. 2b), consistent with the results mentioned in Fig. 1b and 1c. The normalized TPSCI has similar interannual variation to the corresponding PC1s both in P1 and P2, whose correlation coefficient reaches up to 0.95 and 0.88 for P1 and P2, respectively. Moreover, the spatial distribution of snow cover anomaly associated TPSCI (Fig. 3) shows high similarity to that of the EOF1 for both epochs (Fig. 2a and 2b). Thus, the TPSCI reconstructed in the present study could represent the interdecadal change in the interannual connection between the western and eastern TPSCA around 1990.

b. Changed effect of distinct TPSCA patterns on SPEC around 1990

TPSC, which could act as an external forcing, is usually termed as an indicator to the atmospheric circulation (Li et al. 2018). Change in the TPSCA would result in an accordingly adjustment of the atmospheric circulation. Whether the impact of different TPSCA patterns on SPEC experiences an interdecadal change will be addressed in the following subsection.

Figure 4 shows the regressed SPEC anomalies against the spring TPSCA for each epoch. Corresponding to a positive TPSCI in P1, that is, more (less) snow cover over the eastern (western) TP, significant positive precipitation anomalies appear south to the YRV (Fig. 4a), inferring that the juxtaposition of less western TPSC but heavier eastern TPSC inclines to wet spring over the area south to YRV and vice versa. In contrast, in P2, linked to excessive snow cover lying over the whole TP, pronounced negative precipitation anomalies prevail over YRV-HRV with insignificant positive precipitation anomalies south to YRV (Fig. 4b). It suggests that excessive snow covering entire TP tends to dry the YRV-HRV region and vice versa. Upon examination of the regression maps of SPEC anomaly by removing the influence of ENSO (Fig. 4c and 4d), the results bear a strong resemblance to Fig. 4a and 4b, indicating that ENSO may have limited influence on the interannual linkage between the TPSCA and SPEC in the present case.

Another sequent and interesting question is whether the SPEC experiences an interdecadal shift around 1990. As noted by Xu et al. (2019), the location of most remarkable interannual variance of SPEC anomaly shifts from South China to YRV around the mid-1990s. Apart from its variance, whether the anomalies of SPEC possess other characteristics before and after 1990 deserves further investigation.

Fig. 5 displays the first two EOF modes of the interannual variability of SPEC (termed as EOF1_SPEC and EOF2_SPEC, respectively). The EOF1_SPEC, accounting for 28% of the total variance, displays a coherent variation south to YRV, together with relatively weak but significant signals near Shanxi and Sichuan Province (Fig. 5a). The EOF2_SPEC accounts for 14% of the total variance, featured by a meridional opposite pattern between the eastern China south and north to 26°N (Fig. 5b). Furthermore, the interannual variance of PC1 and PC2 seemly exhibits an interdecadal change to some extent (Fig. 5c and 5d). In particular, the PC2 shifts to a relatively active period with large variance after 1990, although it becomes silent again after the middle 2000s (Fig. 5d). The turning point of PC2 around 1990 passes the running F-test at 99% confidence level (Fig. 5f), suggesting the EOF2 may become a domain mode after 1990. The year 1990 is same as the abrupt changed year of TPSCA (Fig. 1c), which may imply that the TPSC change around 1990 may somewhat take effect on the interdecadal change of the SPEC. Why the SPEC changes after the middle 2000s is an interesting question that remains unknown. It is speculated that the spring precipitation anomaly may be modulated by the Pacific Decadal Oscillation (Wu and Mao 2016), however, it is out of our scope.

It is worthwhile to mention that the interannual variance of PC1 is relatively smaller for 1994–2009 compared with other subperiods, despite it is insignificant based on the running F-test technique (Fig. 5e). It indeed favors the EOF2 becomes more dominant after 1990, that is, the rainfall pattern with coherent variation south to YRV (i.e., EOF1_SPEC) would dominate in P1, whereas the rainfall pattern of opposite variation between the South China and the YRV-HRV (i.e., EOF2_SPEC) would switch from a minor in P1 to relatively more important mode in P2. The role of TPSCA on the anomalous SPEC pattern before and after 1990 would be addressed in the following section.

4. Physical Process Of The Modulation Of Tpsca On The Spring Precipitation

It has been demonstrated that a prominent interdecadal shift was observed both in the relationship of snow cover between the western/eastern TP and their effects on the anomalous SPEC pattern around the early 1990s. Meanwhile, the formation of interdecadal changed SPEC anomaly patterns might be partly ascribed in the interdecadal switched signatures of TPSCA. In this section, the physical processes for the TPSCA impact on SPEC are explored for both epochs.

a. Observation

Accumulative evidence has been widely proposed that the TP snow could serve as an atmospheric driver, which will modulate the large-scale atmospheric circulation by diabatic cooling effect (Zhang et al. 2004; Xu et al. 2012; Wang et al. 2018, 2019; Qian et al. 2019). The TPSCA-associated anomalies of atmospheric apparent heat source (Q_1) are shown in Fig. 6 for both subperiods. During P1, an out-of-phase TPSCA pattern with less snow over the western TP but heavier snow over the eastern TP helps to result in a significant heating over the western TP along with a relatively limited cooling over the southeastern TP (Fig. 6a), of which the vertical profile reaches its maximum near the surface of TP, that is, approximately 500hPa (Fig. 6c). However, during P2, an in-phase TPSCA pattern may lead to significant cooling over the entire TP with two anomaly centers lying at 35°N, 84°E and 30°N, 98°E (Fig. 6b), which largely differs from the specific pattern in P1. Accordingly, the profiles of these two cooling centers over the mid-western and eastern TP can be detected from surface to upper tropospheric at 300-hPa, whose intensity basically decreases along altitude, except for the eastern EP cooling lower than 400hPa (Fig. 6d).

To further gain insights into the mechanisms for the impact of TPSCA on anomalous SPEC patterns, the atmospheric circulation anomalies tied to both the in-phase and out-of-phase TPSCA patterns for both epochs are displayed in Fig. 7. During P1, the local response to the out-of-phase TPSCA pattern is featured by a significant anomalous warming anticyclone at 300-hPa prevailing over the western TP and extending to its southwest, together with a prominent TP cold cyclone (TPCC) sweeping over the eastern TP and expanding to the Bay of Bengal and Indochina Peninsula (Fig. 7a). These two activity actions basically locate over the western and southeastern TP, somewhat according with the regions where the largest diabatic heating or cooling anomaly lies (Fig. 6a). In the lower troposphere, corresponding to the out-of-phase TPSCA in P1, the pattern with anomalous western TP anticyclone, northern Bay of Bengal cyclone and western North Pacific anticyclone (anticyclone, cyclone and anticyclone pattern i.e., ACA-like pattern, hereafter) can be detected in P1 (Fig. 7c). This clear ACA-like pattern can also be observed in the middle level (Fig. S1a, in supplementary material). In the ACA-like pattern, the cooccurrence of the anomalous northern Bay of Bengal cyclone and western North Pacific anticyclone induces the anomalous southerly flow sweeping along the coast of East Asia (Fig. 7c). As such, the wet anomalies over the areas south to YRV are more likely to the southerly water vapor flux transporting into that area and the significant ascending motion there.

In contrast, during P2, responding to the in-phase TPSCA pattern, a pronounced TPCC, apparently enlarged and northward-eastward advanced, spans entire TP and extends downstream to the YRV-HRV

(Fig. 7b). Such enlarged and strong TPCC may be largely attributed to the expanded diabatic cooling domains (Fig. 6b), which is directly induced by the heavier snow over most of the TP in P2 (Fig. 3b). This result implies that the TPSCA pattern can significantly modulate the location and spatial scale of the atmospheric circulation (for example, the TPCC and TP anticyclone) responding to the TPSC-induced diabatic cooling or heating. In the lower level, the anomalous westerly can be founded over the YRV-HRV (Fig. 7d). Meanwhile, the westerly can also extend to middle (Fig. S1b) and upper level (Fig. 7b). Along the southern flank of TPCC, the westerly propagates cold and dry air from TP to downstream YRV-HRV (Fig. 7b, Fig. S1b and Fig. 7d). Therefore, the dry anomalies over the YRV-HRV are attributable to the cold and dry air derived from upstream TP accompanied by the sinking motion, which provides a dynamical condition to suppress rainfall.

To further inspect the individual effect of TPSCA over different domains, the atmospheric circulation responses linked to one of the key regions are depicted in Fig. 8 for the first epoch. A below-than-normal western TPSC is associated with a local western TP warm-anticyclone in the upper troposphere (Fig. 8a), and a western TP anticyclone and northern Bay of Bengal cyclone in the lower level (Fig. 8c). However, more eastern TPSC is related to a local eastern TPCC in the upper troposphere (Fig. 8b), and a half of northern Bay of Bengal cyclone and a western North Pacific anticyclone in the lower level (Fig. 8d). Naturally, the response of upper tropospheric circulation to out-of-phase TPSCA is featured by a western TP warm-anticyclone and an eastern TPCC in the upper troposphere (Fig. 7a), and the ACA-like pattern in the lower level (Fig. 7c). In addition, the large warm and cold regions are consistent with the diabatic heating and cooling areas (Fig. 6a), respectively, further indicating that the TPSCA may modulate atmospheric circulation by diabatic heating (cooling) effect.

In contrast, during P2 (Fig. 9), the response of an upper tropospheric cold trough to western TPSCA sweeps over western TP with large cold anomalies lying over mid-western TP (Fig. 9a), and the lower-level westerly response spans entire YRV-HRV (Fig. 9c). Moreover, an upper tropospheric TPCC response to eastern TPSCA prevails over the entire TP with large cold anomalies lying over eastern TP (Fig. 9b), and the lower-level northwesterly and sinking motion response prevails over the YRV-HRV (Fig. 9d). Accordingly, the response of an upper level TPCC to in-phase TPSCA lies over the entire TP with two large cold areas over the mid-western and eastern TP (Fig. 7b), and the lower tropospheric pronounced westerly accompanied by descending motion anomalies lie over the YRV-HRV (Fig. 7d). It may infer that the eastern TPSCA plays a more important role in inducing the SPEC pattern in P2.

Generally, the positive TPSCA, by its local diabatic cooling effect, may stimulate a local anomalous TPCC lying over the TP and extended to its surroundings. The TPSCA associated anomalous SPEC regions, in large measure, hinges on the domain of the TPCC. For P1, since the TPCC centered at the southeastern TP and extended to Bay of Bengal, along its southeastern flank, the southwesterly may propagate warm-wet flow from Bay of Bengal to south to YRV, which accompanied by significant ascending motion favor the rainfall there. Whereas, during P2, as the TPCC enlarged and northward advanced, the westerly, at the southern flank of which, may transport dry-cold flow from TP to YRV-HRV, which accompanied by

pronounced sinking motion inhibit the rainfall there. Thus, the TPCC could serve as an "air bridge" in linking the upstream TPSCA-induced diabatic cooling and downstream SPEC anomalies.

Although such responses of atmospheric configurations to the distinct TPSCA patterns, to a certain extent, can interpret the formation of the downstream precipitation anomalies patterns, it is the statistical relationships to connect the downstream precipitation anomalies with the upstream thermal forcing tied to TPSCA. To further validate the upstream-downstream linkage, we next employed a model simulation to investigate the thermal forcing induced by TPSCA and its circulation response.

b. Numerical Experiments

Previous studies indicate that the LBM can reproduce the atmospheric circulation forced by the TPSCA-induced diabatic heating (Jiang et al. 2016, Jia et al. 2021, Wang et al. 2020). According to the observational results obtained hereinabove, we designed six numerical experiments using the LBM (listed in Table 1) to illustrate the TPSCA-induced diabatic cooling/heating effect on the downstream circulation change in both epochs. All simulations are performed by the time integration method and the accumulated integration time up to 40 days. Amid the output data from LBM, the variables at last 10 days as the stabilizing state are then averaged for further analysis.

Western TP heating anomalies (EXP1) and southeastern TP cooling anomalies (EXP2) were imposed in the LBM with the spring mean flow in P1 (Fig. 10a, 10b), which is used to diagnose the effect of out-of-phase TPSCA pattern on the downstream atmospheric circulation. In EXP3 and EXP4 experiments, the model is operated by adding mid-western TP cooling anomalies (EXP3) and eastern TP cooling anomalies (EXP4) (Fig. 10c, 10d) with the spring basic state in P2. The other detailed set-ups about these experiments (e.g., the elliptical radius, central location, vertical profile etc. listed in Table 1) were determined based on the observations (Fig. 6).

Figure 11 provides the model simulated atmospheric circulations according to the EXP1 and EXP2 experiments in P1. Corresponding to the western TP heating forcing (EXP1), simulative responses seize a clear upper tropospheric local anticyclone overlaid a high-pressure over the western TP (Fig. 11a), and a lower tropospheric anticyclone over the mid-western TP and upward motion over the East China (Fig. 11b), which accords with the western TPSCA induced circulation response in Fig. 8a and Fig. 8c. Moreover, response to the southeastern TP cooling forcing (EXP2), atmospheric responses capture an apparent upper tropospheric local cyclone overlaid a low-pressure over the eastern TP (Fig. 11c), and a lower tropospheric northern Bay of Bengal cyclone and a western North Pacific anticyclone accompanied by upward (downward) motion south (north) to the YRV (Fig. 11d), which are consistent with the eastern TPSCA induced circulation response in Fig. 8b and Fig. 8d. In addition, linearly adding these two experiments, the model results reasonably reoccur the upper tropospheric local anticyclone and cyclone over western and eastern TP (Fig. 11e), and also reproduce the lower-level ACA-like pattern and ascending motion over the area south to YRV (Fig. 11f), which are in keeping with much of the observed panels in Fig. 7a and 7c.

In P2, based on the EXP3 and EXP4, model simulated atmospheric circulations are displayed in Figure 12. Corresponding to the mid-western TP cooling forcing (EXP3), an evident upper tropospheric local cyclone overlaid a low-pressure over the mid-western TP (Fig. 12a), and a lower tropospheric northwesterly accompanied by descending motion over the YRV-HRV (Fig. 12b) are similar with the western TPSCA induced circulation in Fig. 9a and Fig. 9c. Moreover, response to the eastern TP cooling forcing (EXP4), a distinct upper tropospheric local cyclone overlaid a low-pressure over the eastern TP (Fig. 12c), and a lower tropospheric northwesterly accompanied by descending motion over the YRV-HRV (Fig. 12d) are consistent with the eastern TPSCA induced circulation response in Fig. 9b and Fig. 9d. Furthermore, combined these two experiments, the model results seize the upper tropospheric local cyclone over the TP (Fig. 12e), and also reoccur the lower-level westerly and sinking motion over the YRV-HRV (Fig. 12f), which are in keeping with much of the observed panels in Fig. 7b and 7d.

Overall, the model results could reasonably reproduce the TPSCA induced atmospheric circulation systems for both epochs, except some detailed characteristics, e.g., the observed westerly in Fig. 7d is northwesterly in simulated Fig. 12f; and the observed trough in Fig. 9a is low pressure in simulated Fig. 12a. These differences may be attributable to the interference of the other forcing lying in various areas. In general, the model analytical results can further provide supports for the effect of distinct TP heat anomaly on the atmospheric circulation.

Additionally, the southeastern TP cooling forcing experiments in EXP2 (EXP4) and EXP5 (EXP6) were performed by switching the basic state due to similar heating forcing imposed in LBM but with different basic state, which were shown in Fig. S3. Model responses of southeastern (eastern) TP cooling experiments under distinct basic states share high similarity of both the upper tropospheric and lower-level systems. Hence, the differences of atmospheric responses to the eastern TPSCA-induced cooling anomalies were mainly determined by the location and amplitude of the heating forcing, rather than the changed basic state around 1990.

5. Conclusions And Discussions

In the present study, we investigate the interdecadal-changed effect of TP snow cover (TPSC) on spring precipitation over eastern China (SPEC) around 1990. Observational evidence reveals that the relationship in the variability of eastern and western TPSCA switches from out-of-phase during 1970–1989 (P1) to in-phase during 1991–2017 (P2). On account of the interdecadal changes in the TPSCA patterns, the impacts of TPSCA on SPEC follow to experience pronounced shifts from a wet south to YRV pattern in P1 to a dry YRV-HRV pattern in P2. Local diabatic cooling associated with either out-of-phase or in-phase TPSCA relationship could influence the SPEC anomaly by modulating the location and amplitude of the anomalous TP cold-cyclone (TPCC).

Specifically, during P1, the out-of-phase TPSCA, with more snow lying over the eastern TP and less snow to the west, tends to induce a local TPCC anomaly extended southward to north Bay of Bengal in the middle to upper troposphere and a downstream anticyclone anomaly over the western North Pacific in the

lower troposphere, which has been proved by both the observation and model simulations. At southeastern flank of the TPCC and northwestern flank of the western North Pacific anticyclone anomaly, anomalous southwesterly, with apparent signals from upper to lower troposphere, can propagate significant warm-wet flow from Bay of Bengal to south to YRV, favoring the above-than-normal rainfall there.

Differently, the relationship between the western and eastern TPSCA becomes in-phase in P2, namely with excessive TPSCA covering entire TP. Compared with the result in P1, a wider snow cover over the TP leads to an enlarged local cooling anomaly, thereby exciting an expanded and northward-eastward-displaced TPCC anomaly in the middle to upper troposphere. Along the southern flank of such TPCC anomaly, the zonal-distributed westerly could transport dry-cold flow from TP to downstream YRV-HRV, thus inhibiting the rainfall there. Consequently, the effect of TPSCA on the downstream spring rainfall perturbations may be, to a large extent, determined by the TPCC induced by diabatic heating which is closely linked to the TPSC.

The LBM simulation further reveals the time evolution of the TP heating/cooling effect on atmospheric circulation (Fig. S2). During P1, the near surface responses of a sinking motion and an upward motion occur after 2 days in the domains where the cooling and heating forcing are imposed (Fig. S2a). In the subsequent days, the responses are enhanced and eastward propagated with ascending motion appearing over the area south to YRV (Fig. S2b). After about two weeks, the patterns are gradually stable with alternative ascending, descending and ascending motion sweeping over the western TP, eastern TP and south to YRV (Fig. S2c), respectively. Similarly, during P2, the near surface responses of sinking motion appear after 2 days (Fig. S2d), then gradually enhanced and eastward propagated with time (Fig. S2e), and become steady with ascending and sinking motion prevailing over western TP and eastern TP to YRV-HRV (Fig. S2f). The results of the numerical experiments indicate that the anomalous TP diabatic heat can firstly stimulate local atmospheric circulation responses, and then propagate eastward to modulate the downstream atmospheric circulation with time.

Given that the eastern TP diabatic cooling profile in P2 does not strictly decline with altitude (blue curve in Fig. 6d), this implies other forcing may lie in the TPSCA induced diabatic cooling anomalies. To better understanding the TPSCA caused diabatic cooling effect, we design other sensitive experiments utilizing the LBM. Same as the eastern TP cooling experiment in P2 (Fig. 10c), a series of experiments was conducted by changing the cooling profile, in which we transform the altitude of the cooling extremum from surface to upper troposphere. The model responses, with distinct cooling profiles, are very similar to Fig. 12c and Fig. 12d (figure not shown), signifying that the atmospheric responses are insensitive to the cooling profile. Hence, the cooling-induced TPCC in EXP4 is independent of the vertical structure of heat forcing.

It should be mentioned that the rainfall anomalies south to YRV cannot be fully interpreted by the effect of in-phase TPSCA on downstream atmospheric circulation in P2 (compared Fig. 4b and Fig. 5b), which is also true for the LBM simulation (Fig. 12f with feeble vertical motion anomalies south to 28°N).

However, as referred by You and Jia (2018) and Jia et al. (2019), the dipole like SPEC pattern may be also modulated by the sea surface temperature anomaly (SSTA) in the North Atlantic. It infers that the TPSCA acts as only one of the important factors that controls the SPEC variability.

As depicted by You and Jia (2018) in their Fig. 6a-6d, although the SPEC related spring Niño signals are very feeble (see their Fig. 6c), the SPEC associated western North Pacific SSTA can persist from autumn to next summer. Generally, the local negative western North Pacific SSTA, to some extent, hinges on the variability of western North Pacific anticyclone. Whereby, we further removing the spring western North Pacific SSTA to examine whether the TPSC-SPEC relationship is still robust. The response of atmospheric circulation after removing spring western North Pacific SSTA (Fig. S4a-4b) shows very similar to that of removing winter-spring Niño 3.4 (Fig. S4c-4d), confirming that the TPSC-SPEC relationship were still robust even removing western North Pacific SST signals.

Since the relationship of the spring eastern and western TPSC have experienced an interdecadal change, the focus here delves into the effect of different TPSCA pattern on SPEC. Nevertheless, whether the other interdecadal changed forcing, e.g., North Atlantic SSTA, Pacific Decadal Oscillation and North Atlantic Oscillation, contributes to the interdecadal changed SPEC patterns is by no means certain and beyond the scope here. Future work about these issues should be received more attention to further understand the formation of SPEC variability.

Declarations

If any of the sections are not relevant to your manuscript, please include the heading and write 'Not applicable' for that section.

To be used for all articles, including articles with biological applications

Conflicts of interest/Competing interests (Not applicable)

Availability of data and material (snow cover data at http://nsidc.org/data/; precipitation data available at http://data.cma.cn/en/?r=data/index&cid=6d1b5efbdcbf9a58; atmospheric variables available at http://www.esrl.noaa.gov/psd/; sea surface temperature data available at https://www.metoffice.gov.uk/hadobs/hadisst/)

Code availability (Fortran, http://www.fortran-2000.com/; the Grid Analysis and Display System (GrADS), http://cola.gmu.edu/grads/; NCAR Command Language (NCL), https://www.ncl.ucar.edu/)

Authors' contributions (Conceptualization: Chao Zhang, Yuanyuan Guo and Zhiping Wen; Formal analysis and investigation: Chao Zhang, Yuanyuan Guo and Zhiping Wen; Original draft preparation: Chao Zhang; review and editing: Yuanyuan Guo and Zhiping Wen; Supervision: Zhiping Wen)

References

Barnett TP, Dümenil L, Schlese U et al (1988a) The effect of Eurasian snow cover on global climate. Science 239: 504–507. https://doi.org/10.1126/science.239.4839.504

Barnett TP, Dümenil L, Schlese U et al (1989b) The effect of Eurasian snow cover on regional and global climate variations. J Atmos Sci 46: 661–685. https://doi.org/10.1175/1520-0469(1989)046,0661:TEOESC.2.0.CO;2

Brodzik M, and Armstrong R (2013) Northern Hemisphere EASE-grid 2.0 weekly snow cover and sea ice extent. Version 4. National Snow and Ice Data Center, Boulder, CO, digital media. Retrieved from https://nsidc.org/data/docs/daac/nsidc0046_nh_ease_snow_seaice.gd.html

Cheng Z, Qiao Y, Jian M et al (2018) Inter-decadal change of leading pattern of spring rainfall over southern China during 1901–2010. Int J Climatol 38: 3494–3512. https://doi.org/10.1002/joc.5511

Crawford AD, Serreze MC (2016) Does the summer arctic frontal zone influence arctic ocean cyclone activity? J Clim 29: 4977-4993. https://doi.org/10.1175/JCLI-D-15-0755.1

Dickson RE (1984) Eurasian snow cover versus Indian monsoon rainfall-An extension of the Hahn-Shukla results. J Appl meteor 23: 171–173. https://doi.org/10.1175/1520-0450(1984)023<0171:ESCVIM>2.0.CO;2

Fan K, Xu Z, Tian B (2014) Has the intensity of the interannual variability in summer rainfall over South China remarkably increased? Meteor Atmos Phys 124: 23–32. https://doi.org/ 10.1007/s00703-013-0301-5

Feng J, Li J (2011) Influence of El Niño Modoki on spring rainfall over south China. J Geophys Res 116: D13102. https://doi.org/10.1029/2010JD015160

Hahn DG, Shukla J (1976) An apparent relationship between Eurasian snow cover and Indian monsoon rainfall. J Geophys Res 33: 2461–2462. https://doi.org/10.1175/1520-0469(1976)033<2461:AARBES>2.0.CO;2

Jia XJ, You. YJ, Wu RG et al (2019) Interdecadal changes in the dominant modes of the interannual variation of spring precipitation over China in the mid-1980s. J Geophys Res 124: 10676– 10695. https://doi.org/10.1029/2019JD030901

Jia XJ, Zhang C, Wu RG et al (2021) Influence of Tibetan Plateau autumn snow cover on interannual variations in spring precipitation over eastern China. Clim Dyn 56: 1-16. https://doi.org/10.1007/s00382-020-05497-8

Jin R, Wu ZW, Zhang P (2018) Tibetan Plateau capacitor effect during the summer preceding ENSO: from the Yellow River climate perspective. Clim Dyn 51: 57–71. https://doi.org/ 10.1007/s00382-017-3906-4

Jiang X, Li Y, Yang S et al (2016) Interannual variation of summer atmospheric heat source over the Tibetan Plateau and the role of convection around the western maritime continent. J Clim 29: 121-138. https://doi.org/10.1175/JCLI-D-15-0181.1

Kalnay E, Kanmitsu M, Kistler R et al (1996) The NCEP/NCAR 40-year reanalysis project. Bull Amer Meteor Soc **77**: 437-470. http://www.esrl.noaa.gov/psd/

Li W, Guo W, Qiu B et al (2018) Influence of Tibetan Plateau snow cover on East Asian atmospheric circulation at medium-range time scales. Nature Commun 9: 4243. https://doi.org/10.1038/s41467-018-06762-5

Lin H, Wu ZW (2011a) Contribution of the autumn Tibetan Plateau snow cover to seasonal prediction of North American winter temperature. J Clim 24: 2801–2813. https://doi.org/10.1175/2010JCLI3889.1

Lin H, Wu ZW (2012b) Contribution of Tibetan Plateau snow cover to the extreme winter conditions of 2009/10. Atmos-Ocean 50: 86–94. https://doi.org/10.1080/07055900.2011.649036.

Rayner NA, Parker DE, Horton EB et al (2003) Global analyses of sea surface temperature, sea ice, and night marine air temperature since the late nineteenth century. J Geophys Res 108(D14): 4407. https://doi.org/10.1029/2002JD002670

Robinson DA, Estilow TW, NOAA CDR Program (2012) NOAA Climate Data Record (CDR) of Northern Hemisphere (NH) snow cover extent (SCE), version 1. [1972–2009]. NOAA National Centers for Environmental Information. https://doi.org/10.7289/V5N014G9

Qian W, Lee DK (2000) Seasonal march of Asian summer monsoon. Int J Climatol, 20: 1371–1386. https://doi.org/10.1002/1097-0088(200009)20:11,1371::AID-JOC538.3.0.CO;2-V

Qian Q, Jia XJ, Wu RG (2019) Changes in the Impact of the Autumn Tibet Plateau Snow Cover on the Winter Temperature over North America in the mid-1990s. J Geophys Res 124(19): 10321–10343, https://doi.org/10.1029/2019JD030245

Si D, Ding YH (2013) Decadal Change in the Correlation Pattern between the Tibetan Plateau Winter Snow and the East Asian Summer Precipitation during 1979–2011. J Clim 26: 7622-7634, https://doi.org/10.1175/JCLI-D-12-00587.1.

You Y, Jia XJ (2018) Interannual variations and prediction of spring precipitation over China. J Clim 31: 655–670. https://doi.org/10.1175/JCLI-D-17-0233.1

Xu X., Guo J., Koike T et al (2012) "Downstream effect" of winter snow cover over the eastern Tibetan Plateau on climate anomalies in East Asia. J Meteor Soc Japan 90C: 113–130. https://doi.org/10.2151/jmsj.2012-C08

Xu C, Qiao Y, Jian M (2019) Interdecadal Change in the Intensity of Interannual Variation of Spring precipitation over eastern China and Possible Reasons. J Clim 32: 5865–5881. https://doi.org/10.1175/JCLI-D-18-0351.1

Yang FL, Lau KM (2004) Trend and variability of China precipitation in spring and summer: Linkage to sea-surface temperatures. Int J Climatol 24: 1625–1644. https://doi.org/ 10.1002/joc.1094

Yasunari T, Kitoh A, Tokioka T (1991) Local and remote responses to excessive snow mass over Eurasia appearing in the northern spring and summer climate. J Meteor Soc Japan 69: 473–487. https://doi.org/10.2151/jmsj1965.69.4_473

Yanai M, Esbensen S, Chu JH (1973) Determination of bulk properties of tropical cloud clusters from large-scale heat and moisture budgets. J Atmos Sci 30: 611–627. https://doi.org/10.1175/1520-0469(1973)030<0611:dobpot>2.0.co;2

Yang K, Guo X, He J et al (2011) On the climatology and trend of the atmospheric heat source over the Tibetan Plateau: An experiments-supported revisit. J Clim 24: 1525–1541. https://doi.org/10.1175/2010JCLI3848.1

Watanabe M, Kimoto M (2000) Atmosphere-ocean thermal coupling in the North Atlantic: A positive feedback. Quart J Roy Meteor Soc 126: 3343–3369. https://doi.org/10.1002/qj.49712657017

Wang Z, Wu RG, Zhao P et al (2019) Formation of Snow Cover Anomalies Over the Tibetan Plateau in Cold Seasons. J Geophys Res 124: 4873-4890. https://agupubs.onlinelibrary.wiley.com/doi/abs/10.1029/2018JD029525

Wang Z, Wu RG, Chen S et al (2018) Influence of western Tibetan Plateau summer snow cover on East Asian summer rainfall. J Geophys Res 123: 2371–2386. https://doi.org/10.1002/2017JD028016

Wang Z, Wu RG, Duan AM et al (2020) Influence of Eastern Tibetan Plateau spring snow cover on North American air temperature and its interdecadal change. J Clim 33: 5123–5139. https://doi.org/10.1175/jcli-d-19-0455.1

Wu X, Mao J (2016) Interdecadal modulation of ENSO-related spring rainfall over South China by the Pacific Decadal Oscillation. Clim Dyn 47: 3203–3220. https://doi.org/10.1007/s00382-016-3021-y

Wu ZW, Jiang Z, Li J et al (2012a) Possible association of the western Tibetan Plateau snow cover with the decadal to interdecadal variations of northern China heatwave frequency. Clim Dyn 39: 2393–2402. https://doi.org/10.1007/s00382-012-1439-4

Wu ZW, Li J, Jiang Z et al (2012b) Modulation of the Tibetan Plateau snow cover on the ENSO teleconnections: From the East Asian summer monsoon perspective. J Clim 25: 2481–2489. https://doi.org/10.1175/JCLI-D-11-00135.1

Wu X, Mao J (2016) Interdecadal modulation of ENSO related spring rainfall over South China by the Pacific Decadal Oscillation. Clim Dyn 47: 3203–3220. https://doi.org/10.1007/s00382-016-3021-y

Xiao Z, Duan AM (2016) Impacts of Tibetan Plateau snow cover on the interannual variability of the East Asian summer monsoon. J Clim 29: 8495–8514. https://doi.org/10.1175/JCLI-D-16-0029.1

Zhang C, Jia XJ, Wen ZP (2021) Increased impact of the Tibetan Plateau Spring Snow Cover to the Meiyu Rainfall over the Yangtze River Valley after 1990s. J Clim. https://doi.org/10.1175/JCLI-D-21-0009.1

Zhang YS, Li T, Wang B (2004) Decadal change of the spring snow depth over the Tibetan Plateau: The associated circulation and influence on the East Asian summer monsoon. J Clim 17: 2780–2793. https://doi.org/10.1175/1520-0442(2004)017,2780:DCOTSS.2.0.CO;2

Zhu Z, Li T, He J (2014) Out-of-phase relationship between boreal spring and summer decadal rainfall changes in southern China. J Clim 27: 1083–1099. https://doi.org/10.1175/JCLID-13-00180.1
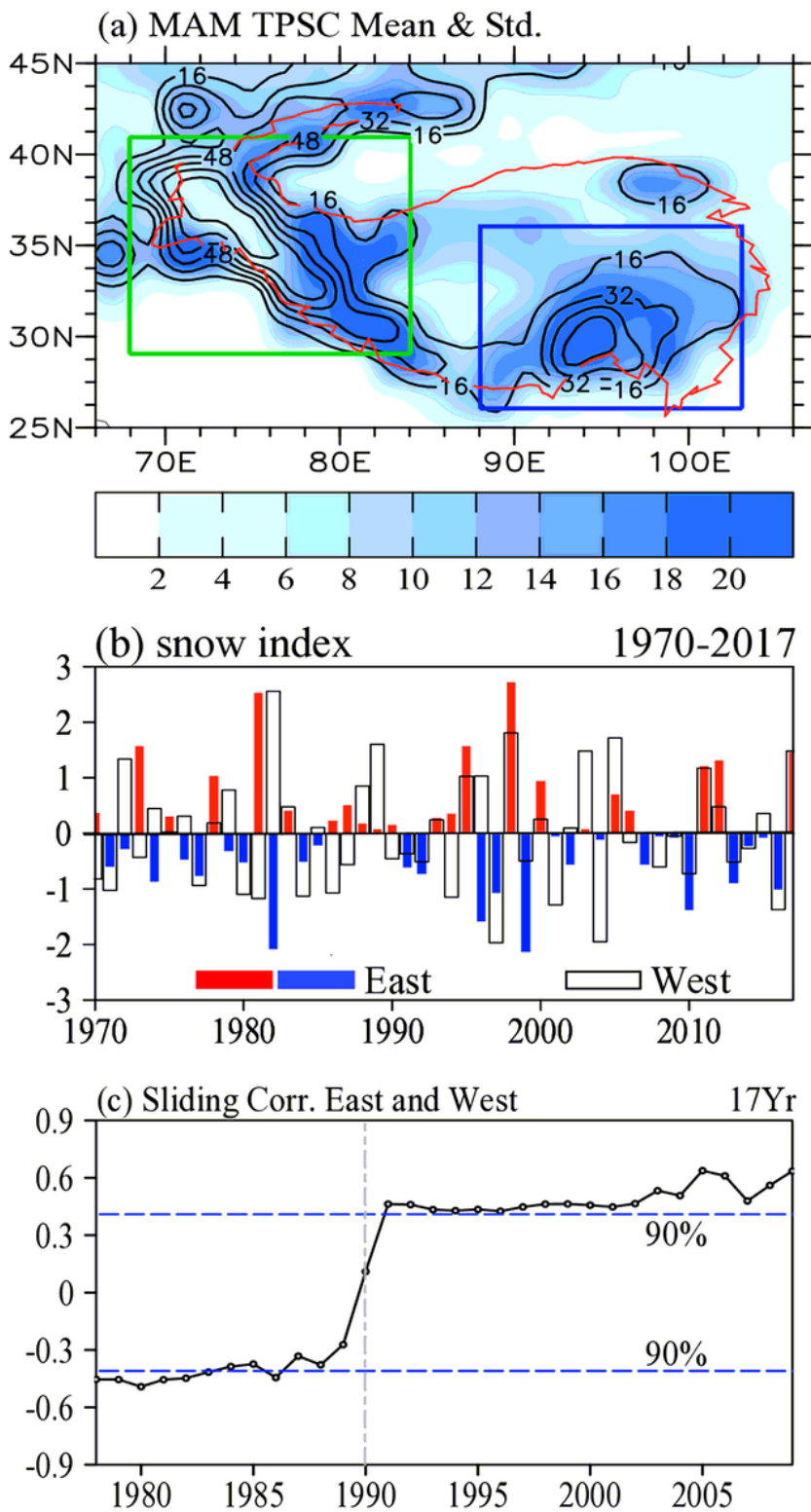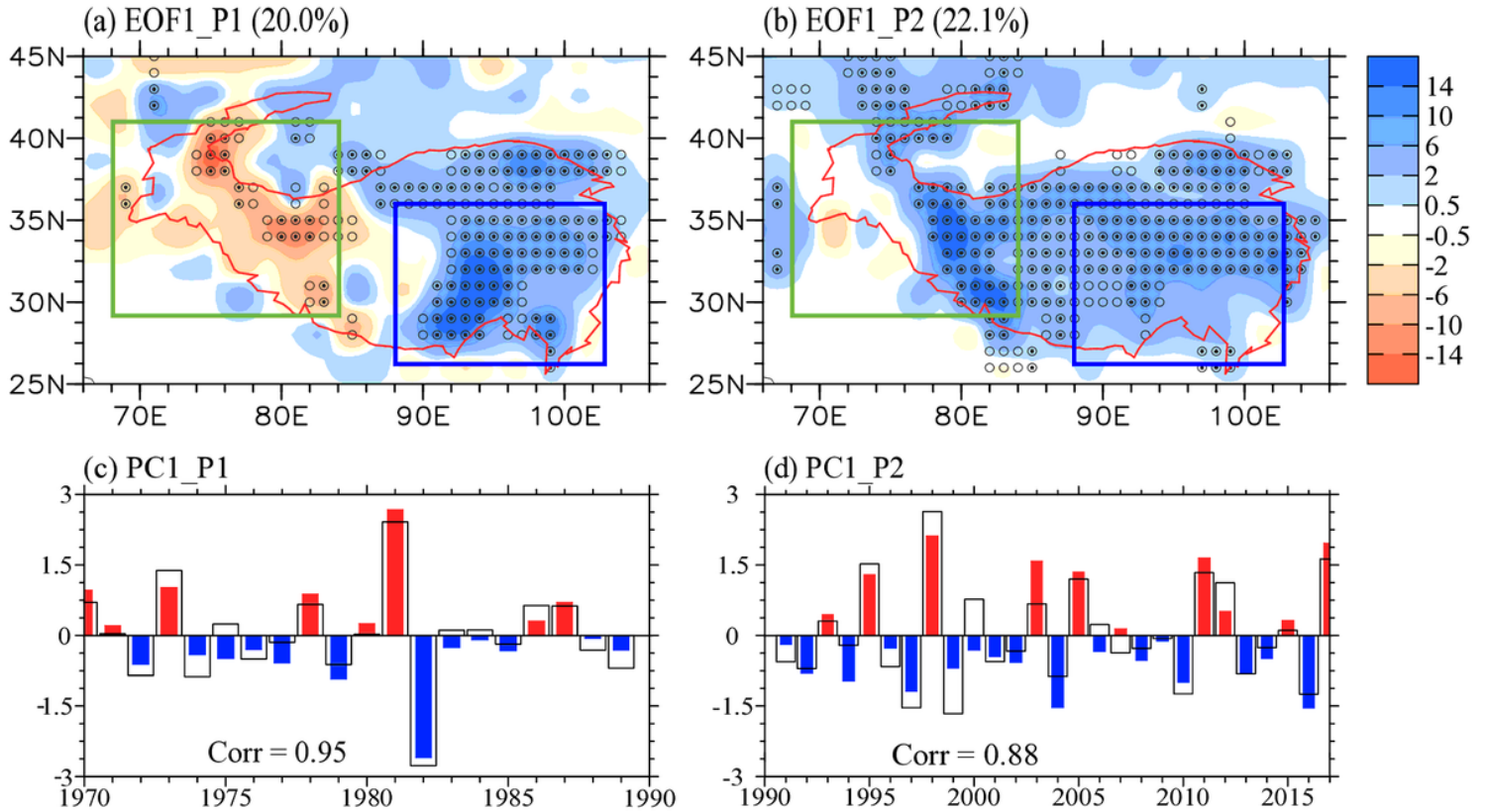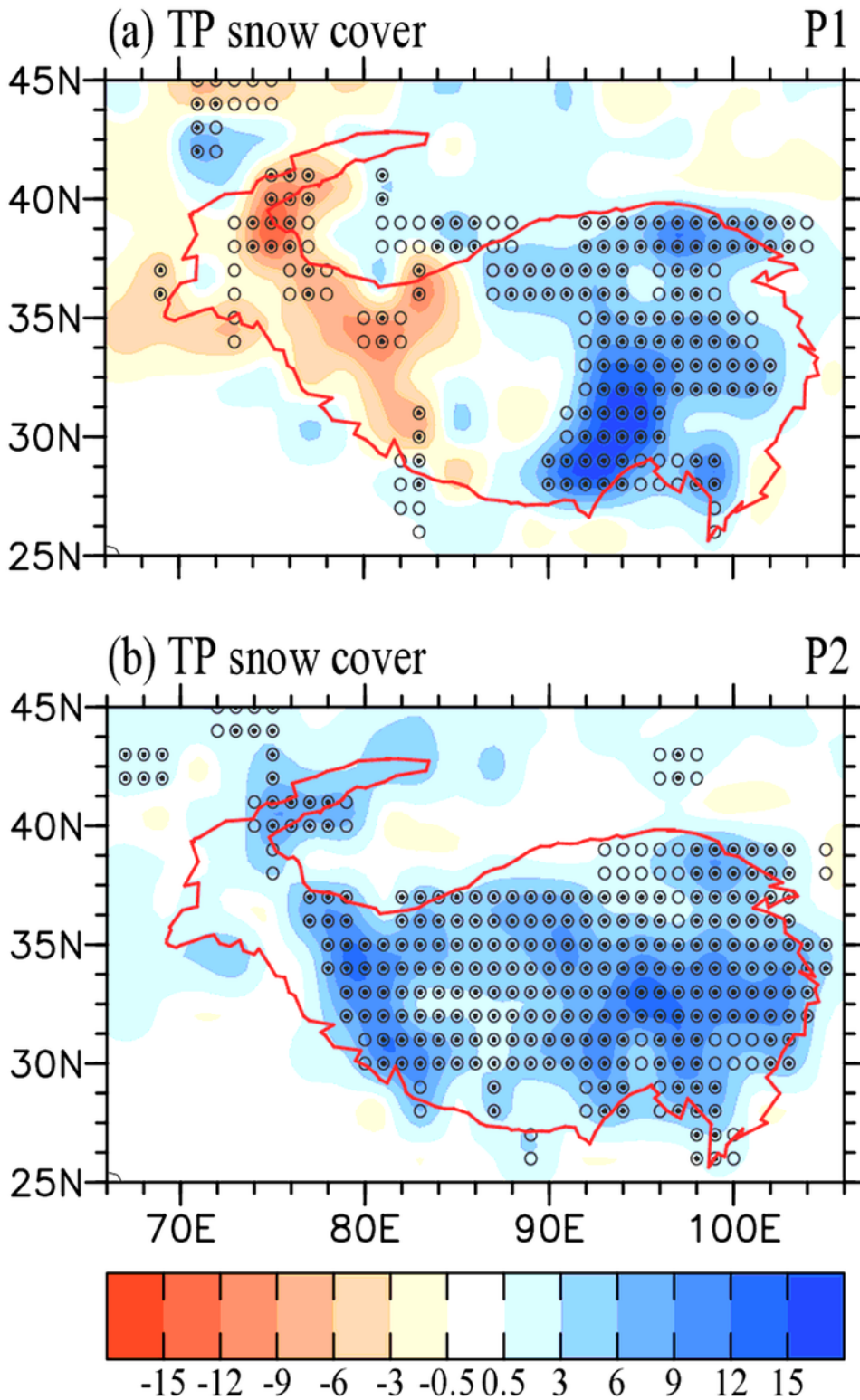
Figures

Figure 1

(a) Spatial distribution of the interannual standard deviation (shading, unit: %) of spring (March-April-May, MAM) TP snow cover (SC) and its climatological mean (contour, unit: %) spanning 1970-2017. (b) The transparent and solid bars refer to the area weighted interannual SC indices over the western (green rectangle in (a): 68-84°E, 29-41°N) and eastern TP (blue rectangle in (a): 88-103°E, 26-36°N), respectively.

(c) The 17-year sliding temporal correlation coefficients (TCCs) between the western and eastern TP SC indices. The threshold of confidence level of 90% of TCCs is marked by the horizonal blue dashed lines.

Figure 2

(a, b) The first leading EOF (EOF1) mode for the interannual variability of TPSC in spring and (c, d) its principal component (PC1, color bars) during (a, c) P1 and (b, d) P2. The transparent bars in (c) and (d) refer to the reconstructed TPSC indices (TPSCI, i.e., eastern area averaged TPSC minus western in P1, but area mean of eastern and western in P2) for P1 and P2, respectively. The green and blue rectangles in (a, b) as in Figure 1a denote the western and eastern TP, respectively. The transparent and solid dotted areas in (a, b) denote the anomalous TPSC exceed the statistical significance level of 90% and 95%, respectively.

Figure 3

Anomalies of spring TPSC (unit: %) obtained by regressing upon the TPSCI for (a) P1 and (b) P2. The transparent and solid dotted areas denote the anomalous TPSC exceed the statistical significance level of 90% and 95%, respectively.
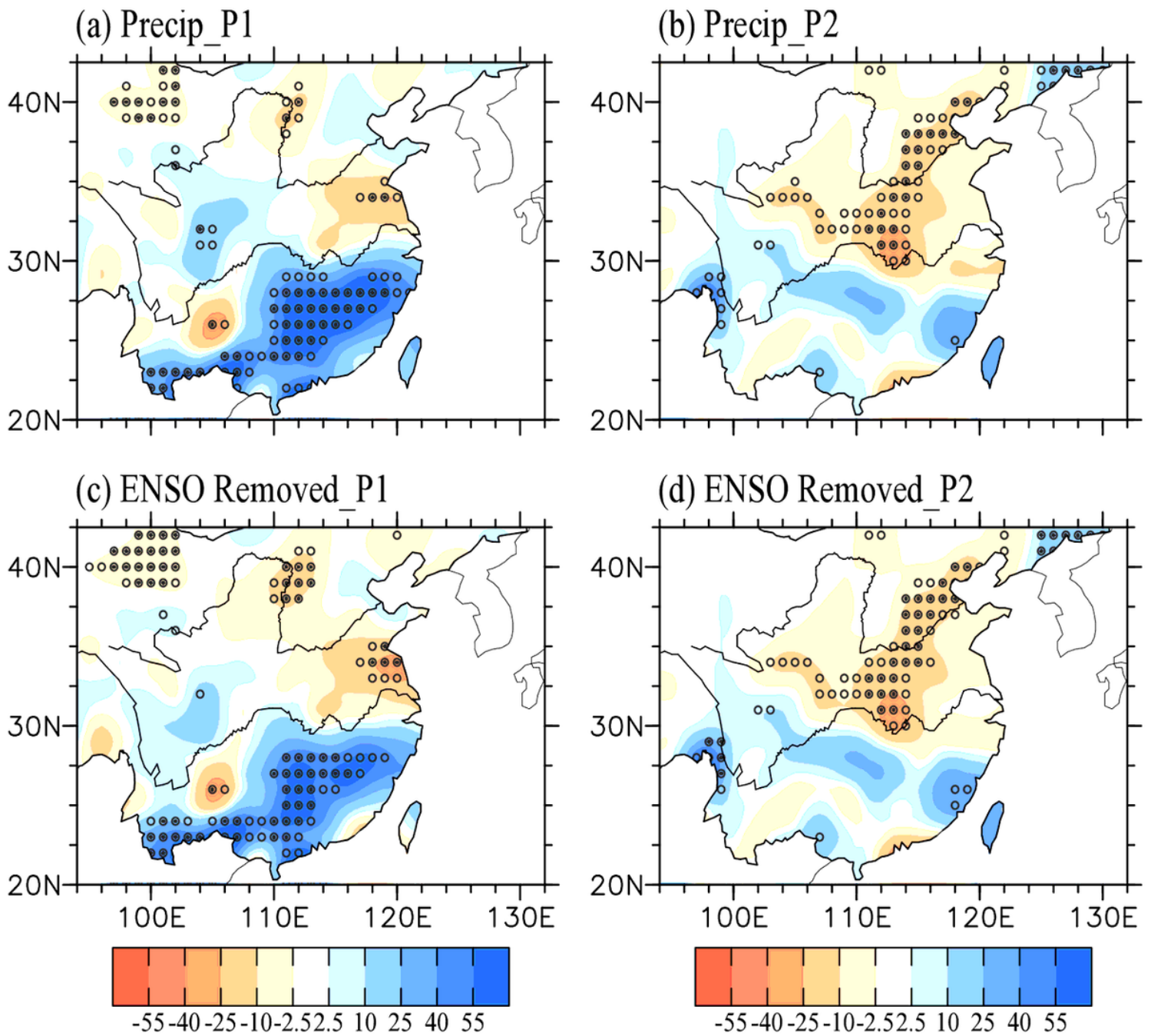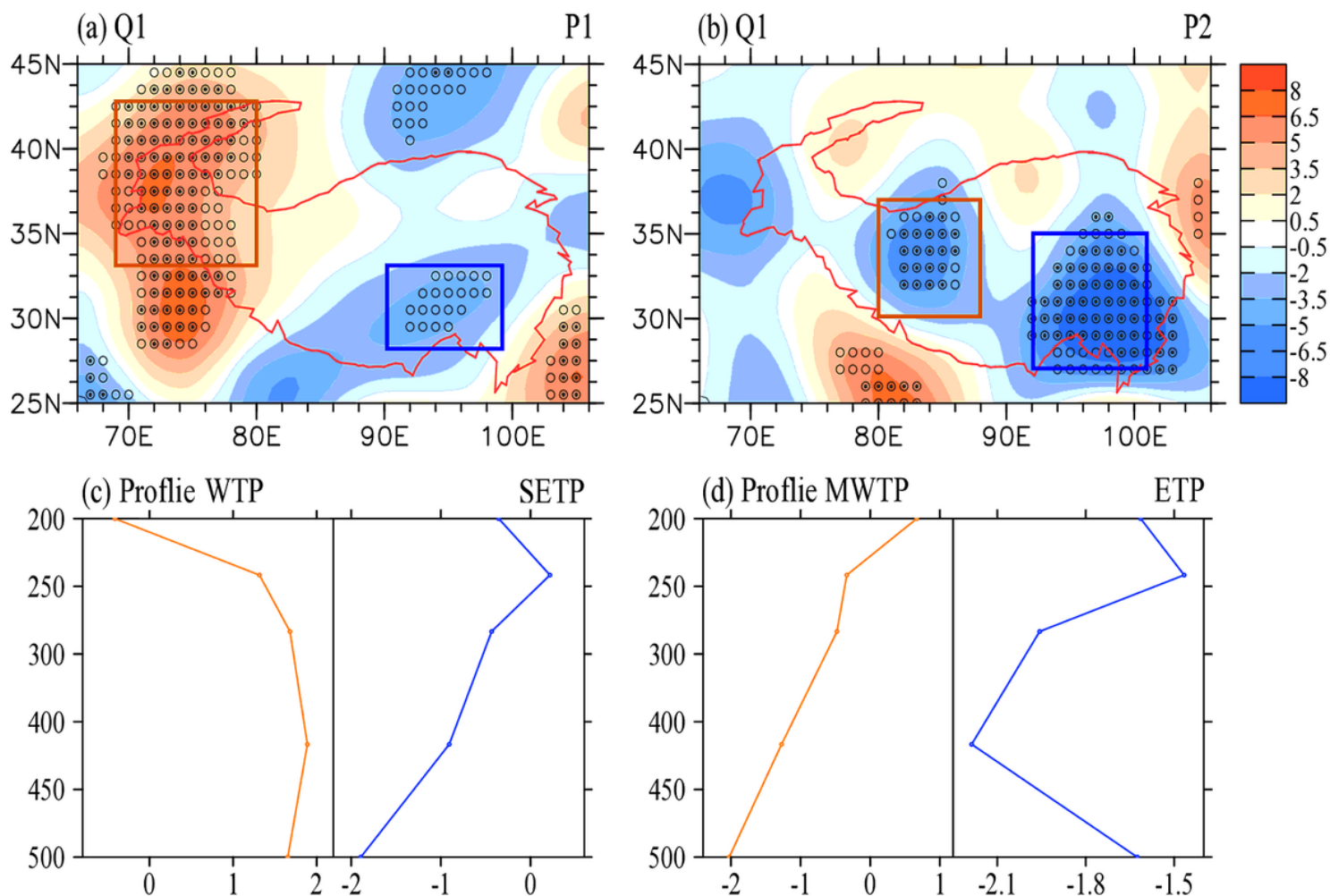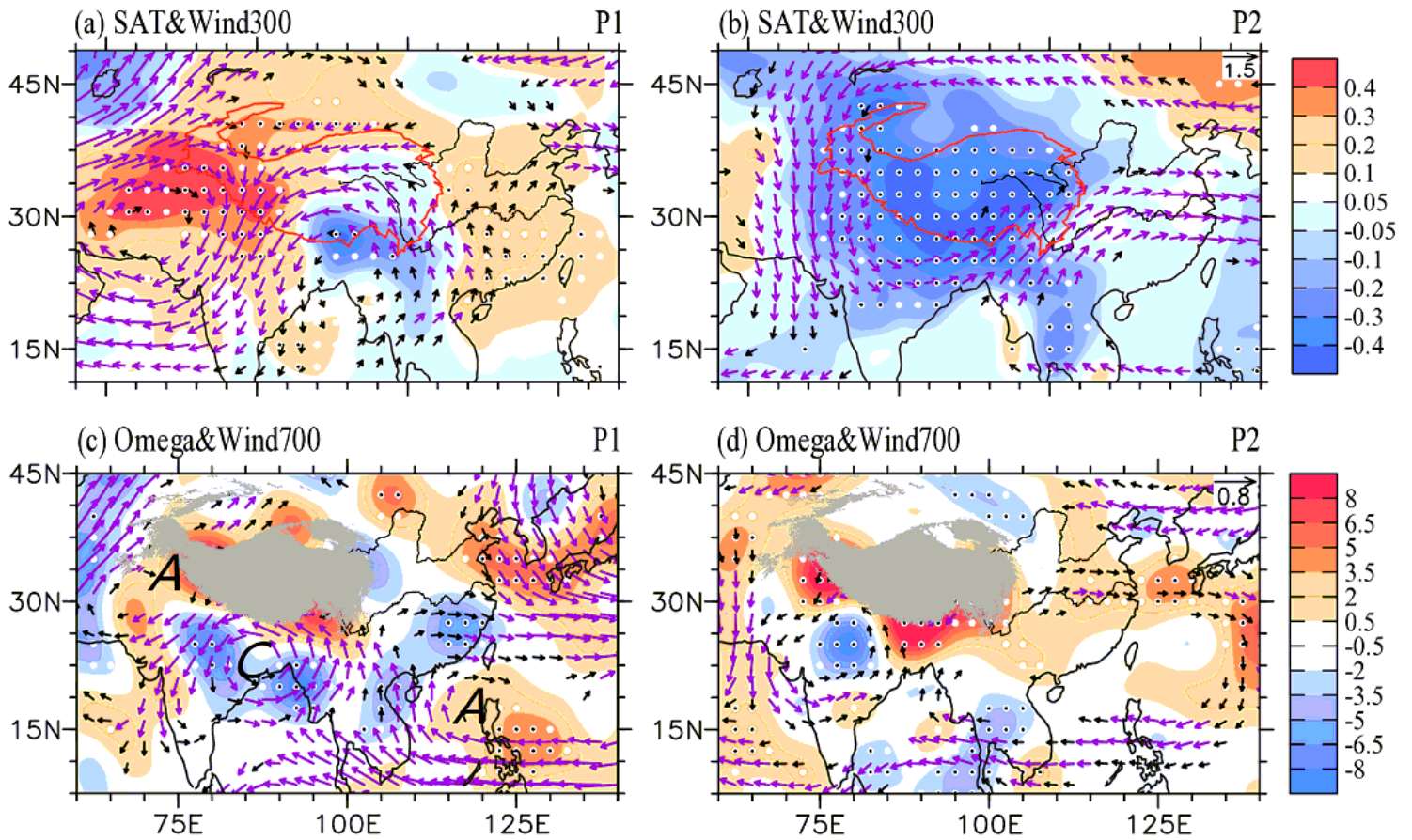
Figure 4

(a) Anomalous spring precipitation (unit: mm/month) over southern China (SPEC) obtained by regressing against the TPSCI for (a) P1 and (b) P2. (c, d) As in (a, b) but for partial regression after removing winter-spring Nino 3.4 signals. The transparent and solid dotted areas refer to the anomalous SPEC exceed the statistical significance level of 90% and 95%, respectively.
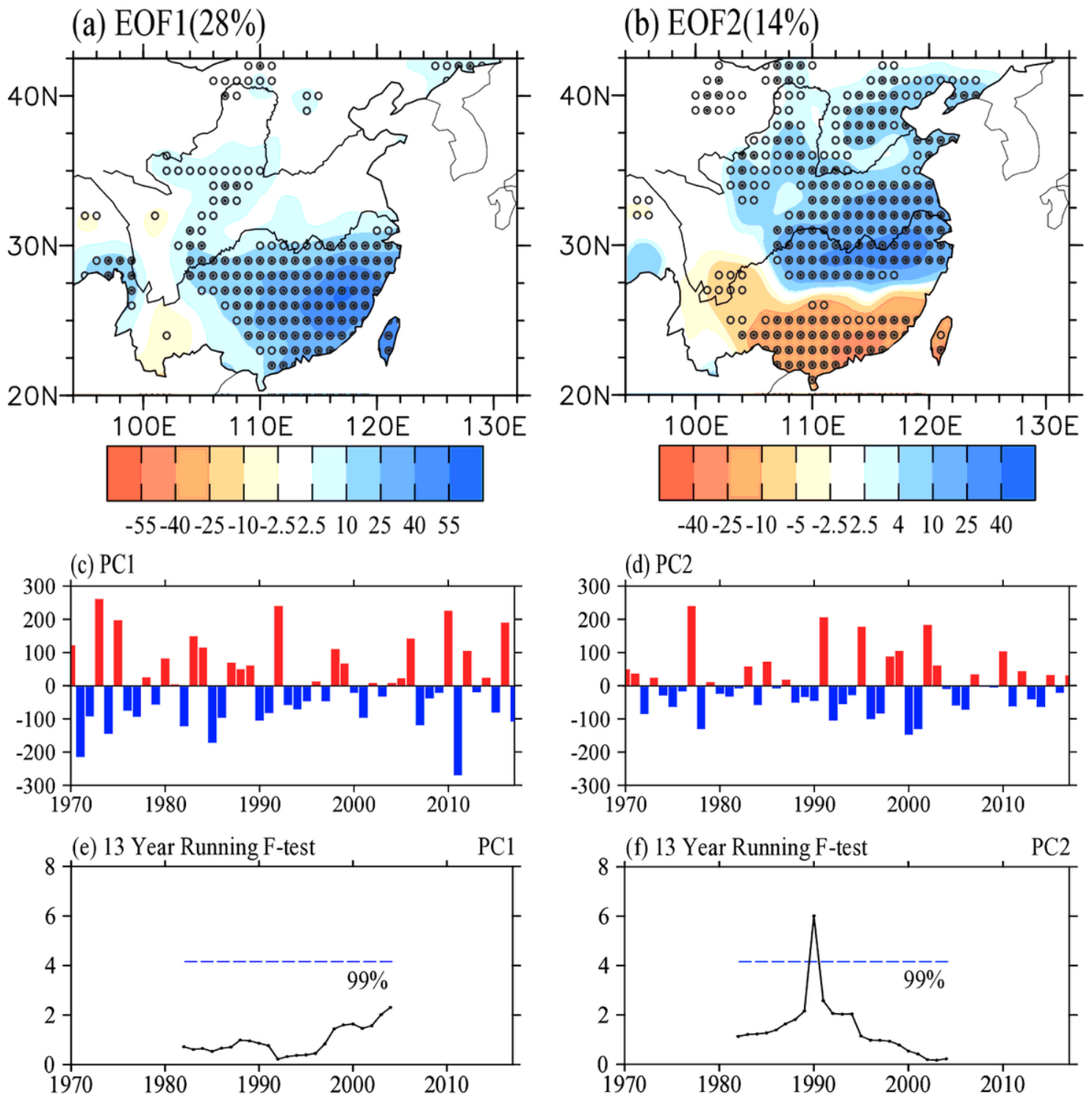
Figure 5

The first two EOF panels of the interannual variability of SPEC for (a) EOF1 and (b) EOF2, and (c, d) its corresponding time series of the principal component. (e, f) The running-F test, with 13-year window, for time series in (c, d). The threshold of confidence level of 99% in (e, f) is marked by the horizonal blue dashed lines. The transparent and solid dotted areas in (a, b) refer to the anomalous SPEC exceed the statistical significance level of 95% and 99%, respectively.

Figure 6

Spatial patterns of spring Q1 (unit: W/m2) anomalies derived from the linear regression against the TPSCI during (a) P1 and (b) P2, and (c, d) the corresponding vertical profile obtained by area mean of Q1 anomalies over the rectangle regions in (a, b). The brow and blue curves in (c, d) refer to the profile over the brow and blue box in (a, b), respectively. The transparent and solid dotted areas refer to the anomalous Q1 exceed the statistical significance level of 90% and 95%, respectively.

Figure 7

Anomalies of (a, b) spring surface air temperature (shading, unit: °C) and wind (vector, unit: m/s) at 300-hPa, (c, d) omega (unit: $10^{-3} \times Pa/s$) at 500-hPa and wind (vector, unit: m/s) at 700-hPa made by partial regression against the TPSCI after removing winter-spring Nino 3.4 signals during (a, c) P1 and (b, d) P2. The scale for the wind vector is displayed at the top-right flank of each panel. The white and dark stippling areas denote the anomalous surface air temperature in (a, b) and omega in (c, d) exceed the statistical significance level of 90% and 95%, respectively. The dark and purple vectors indicate the anomalous wind exceed the statistical significance level of 90% and 95%, respectively.
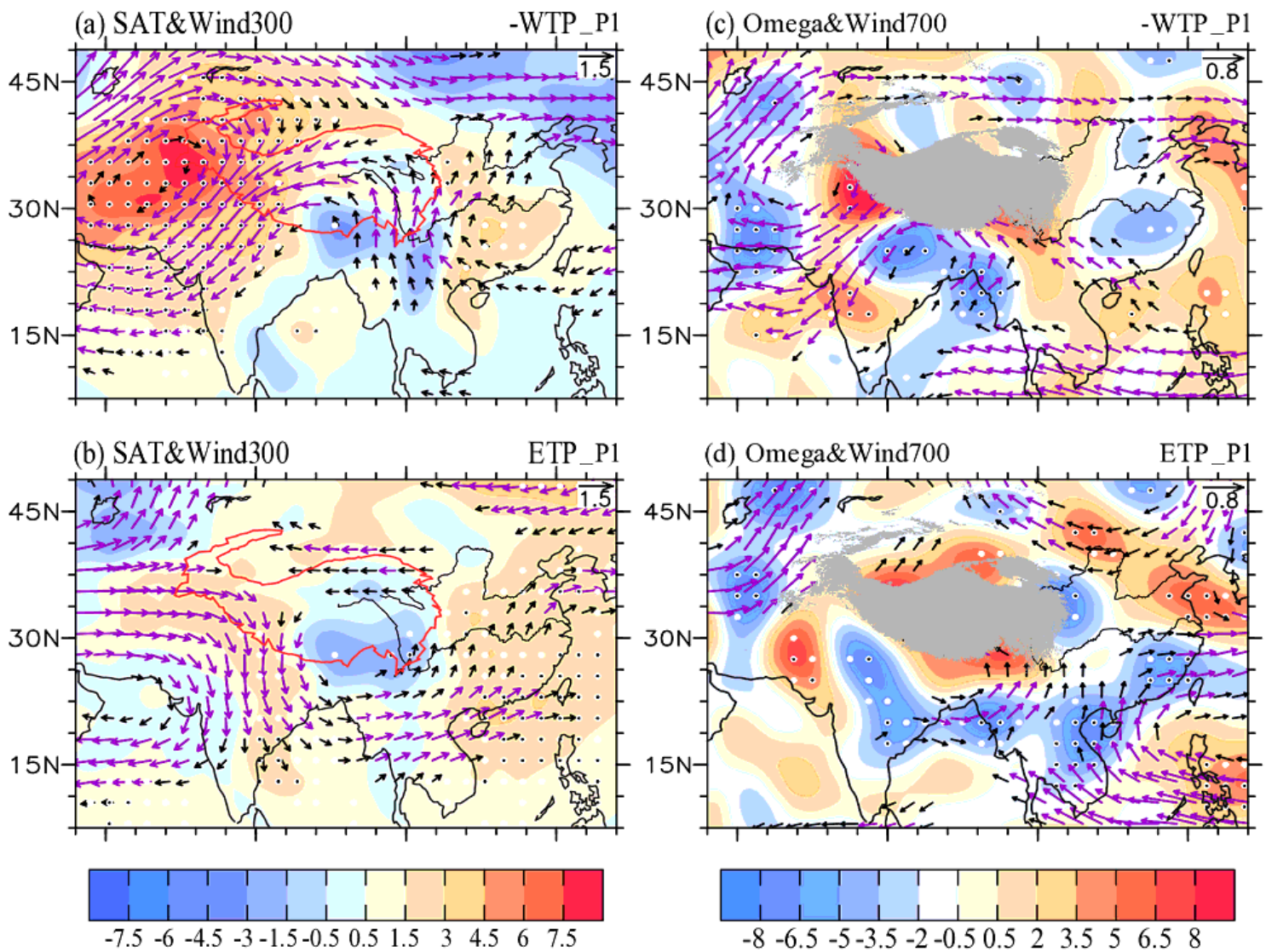
Figure 8

Anomalies of (a, b) spring surface air temperature (shading, unit: $10^{-1} \times °C$) and wind (vector, unit: m/s) at 300-hPa, (c, d) omega (unit: $10^{-3} \times Pa/s$) at 500-hPa and wind (vector, unit: m/s) at 700-hPa obtained by partial regression against the (a, c) negative western TPSC index, and (b, d) eastern TPSC index after removing winter-spring Nino 3.4 signals during P1. The scale for the wind vector is displayed at the top-right flank of each panel. The white and dark stippling areas denote the anomalous surface air temperature in (a, b) and omega in (c, d) exceed the statistical significance level of 90% and 95%, respectively. The dark and purple vector indicate the anomalous wind exceed the statistical significance level of 90% and 95%, respectively.
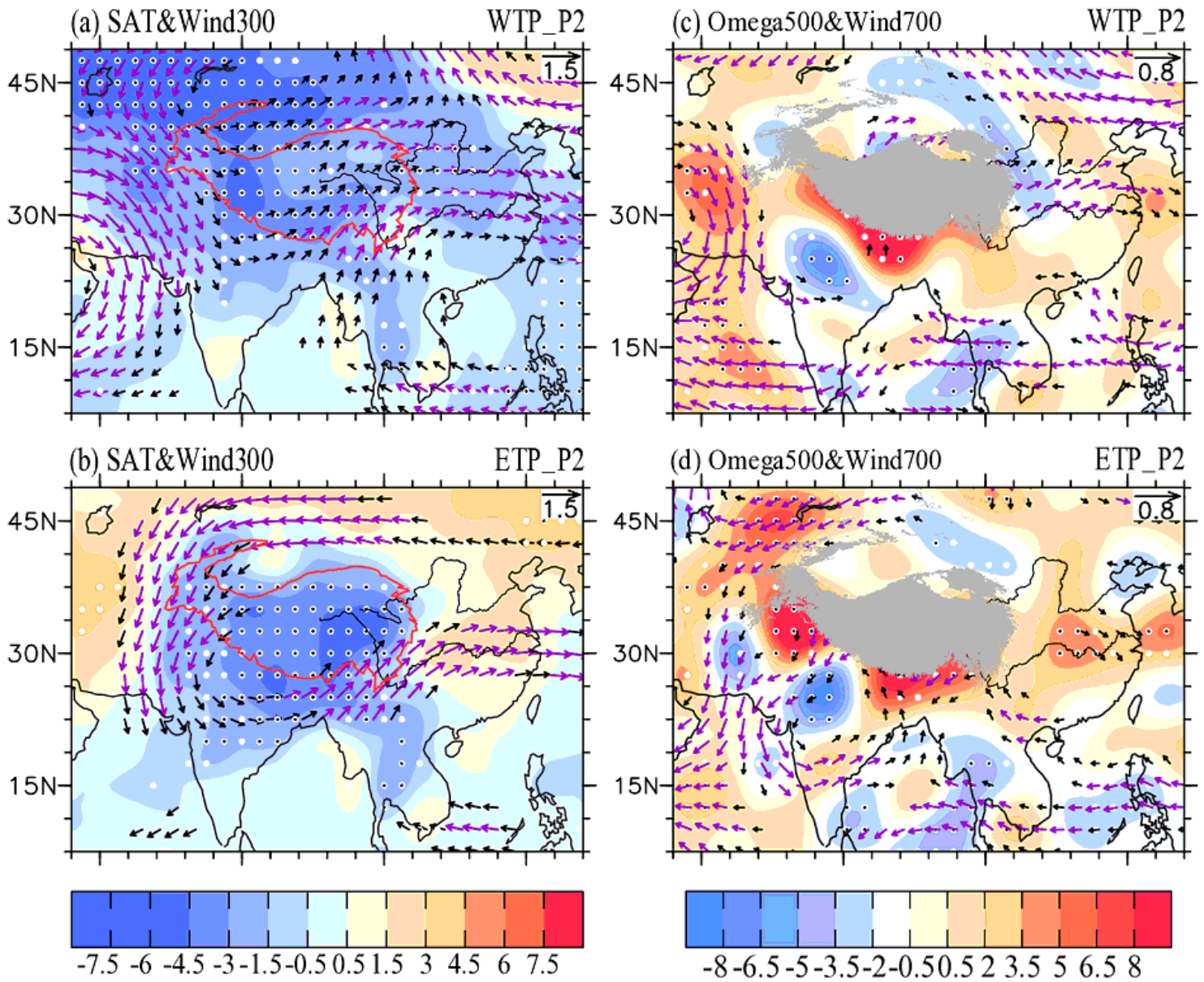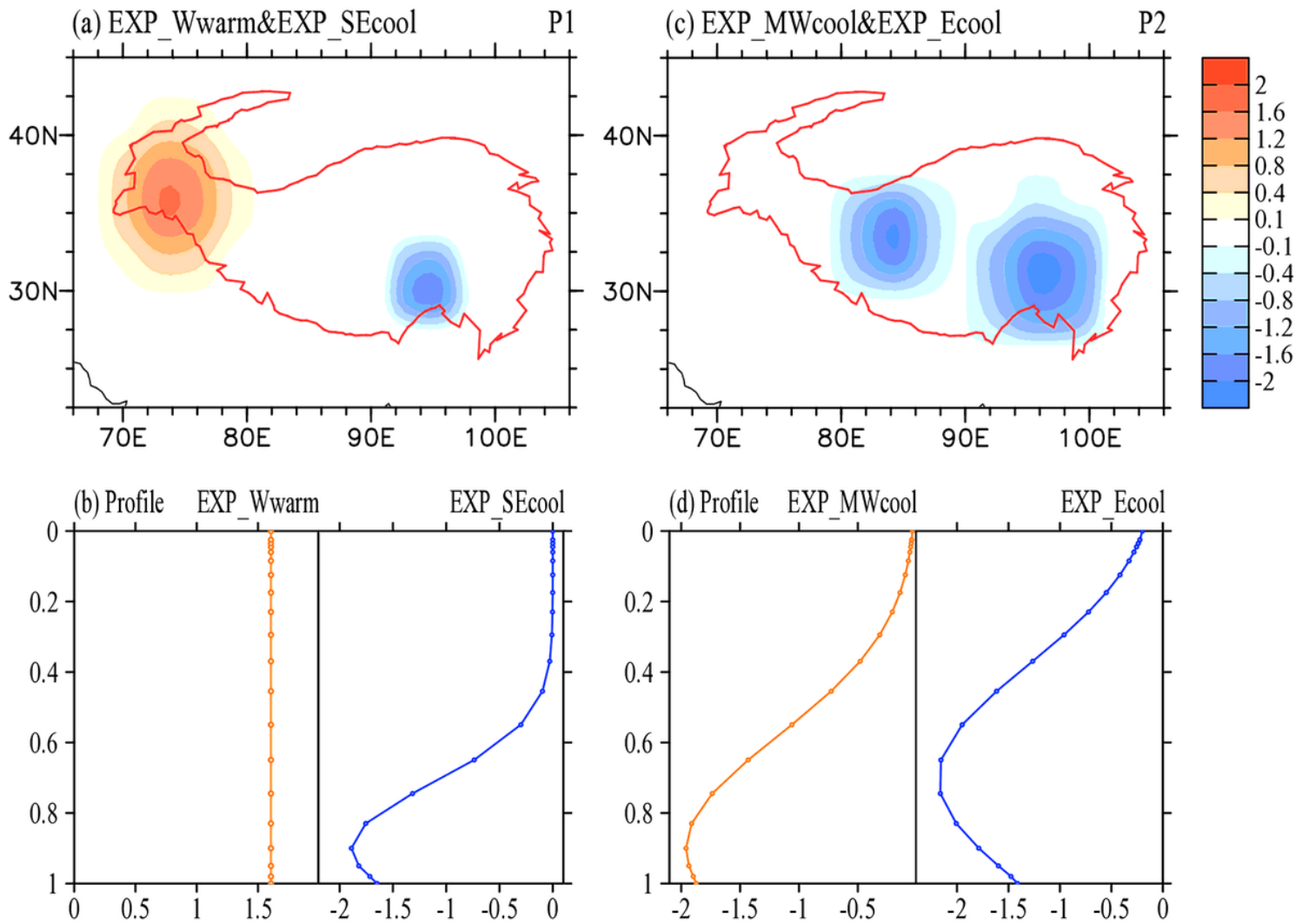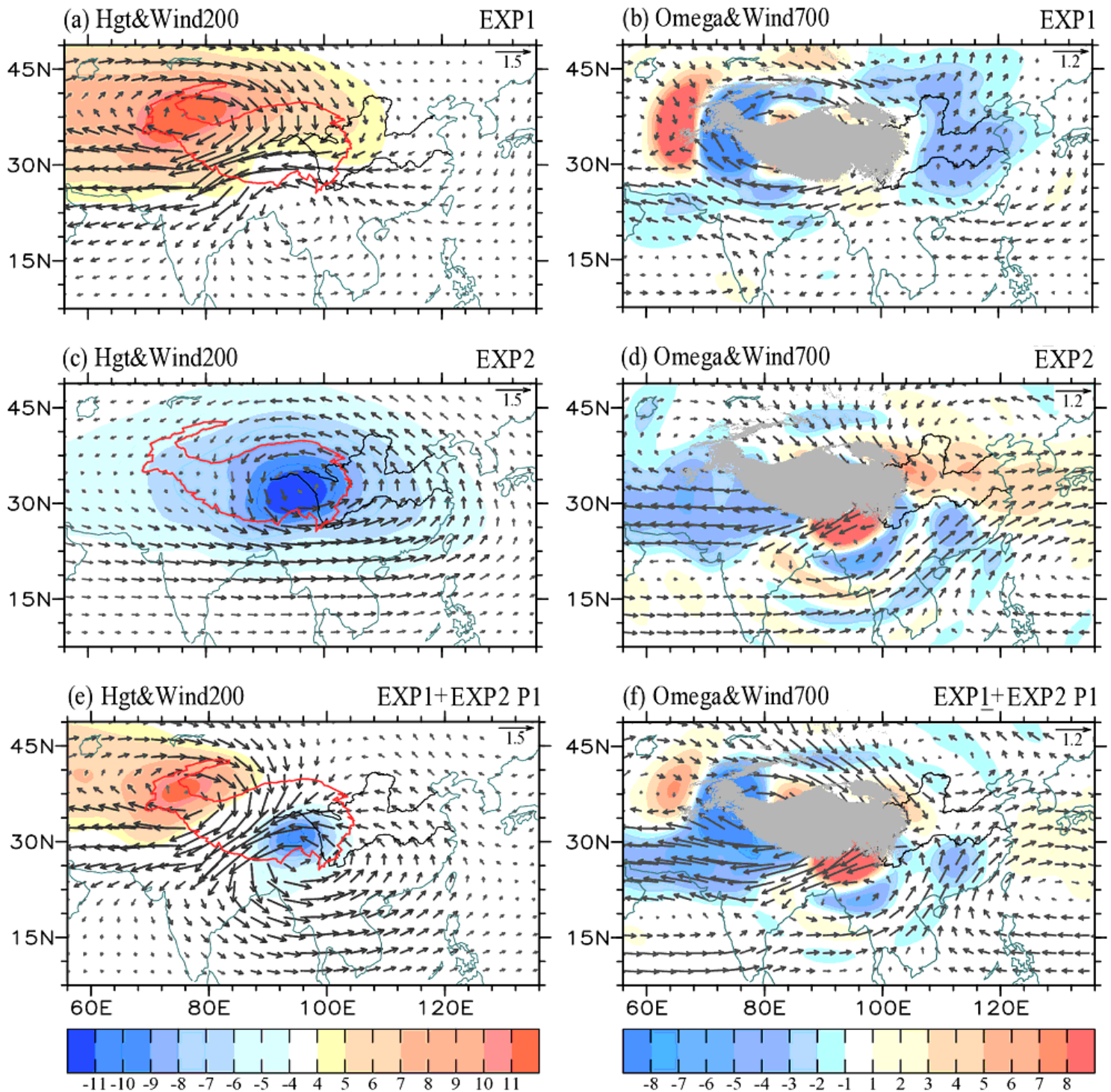
Figure 9

Same as in Figure 8, but for P2.

Figure 10

The spatial distribution of the heating/cooling forcing (shading, unit: K/day) for the basic state of (a) P1 and (c) P2. The yellow and blue shadings in (a) refer to the experiments of western TP heating (EXP1) and southeastern TP cooling (EXP2) at sigma level of 0.9, respectively. The left and right blue shadings in (c) denote the experiments of mid-western TP cooing (EXP3) at sigma level of 0.9 and eastern TP cooling (EXP4) at sigma level of 0.7, respectively. The curves in (b) with brown and blue refer to the profile of EXP1 and EXP2, respectively. Whereas the curves in (d) with brown and blue denote the profile of EXP3 and EXP4, respectively.

Figure 11

Simulated atmospheric response to the idealized TP forcing added to the climatological spring basic flow for the (a, b) EXP1, (c, d) EXP2, and (e, f) EXP1 + EXP2 during the basic state of P1. The response of (a, c, e) geopotential height (unit: gpm) and wind (vector, m/s) at 200-hPa, and (b, d, f) vertical velocity (unit: 10-3×Pa/s) and wind (vector, m/s) at 700-hPa. The scale for the wind vector is depicted at the top-right flank in each panel.
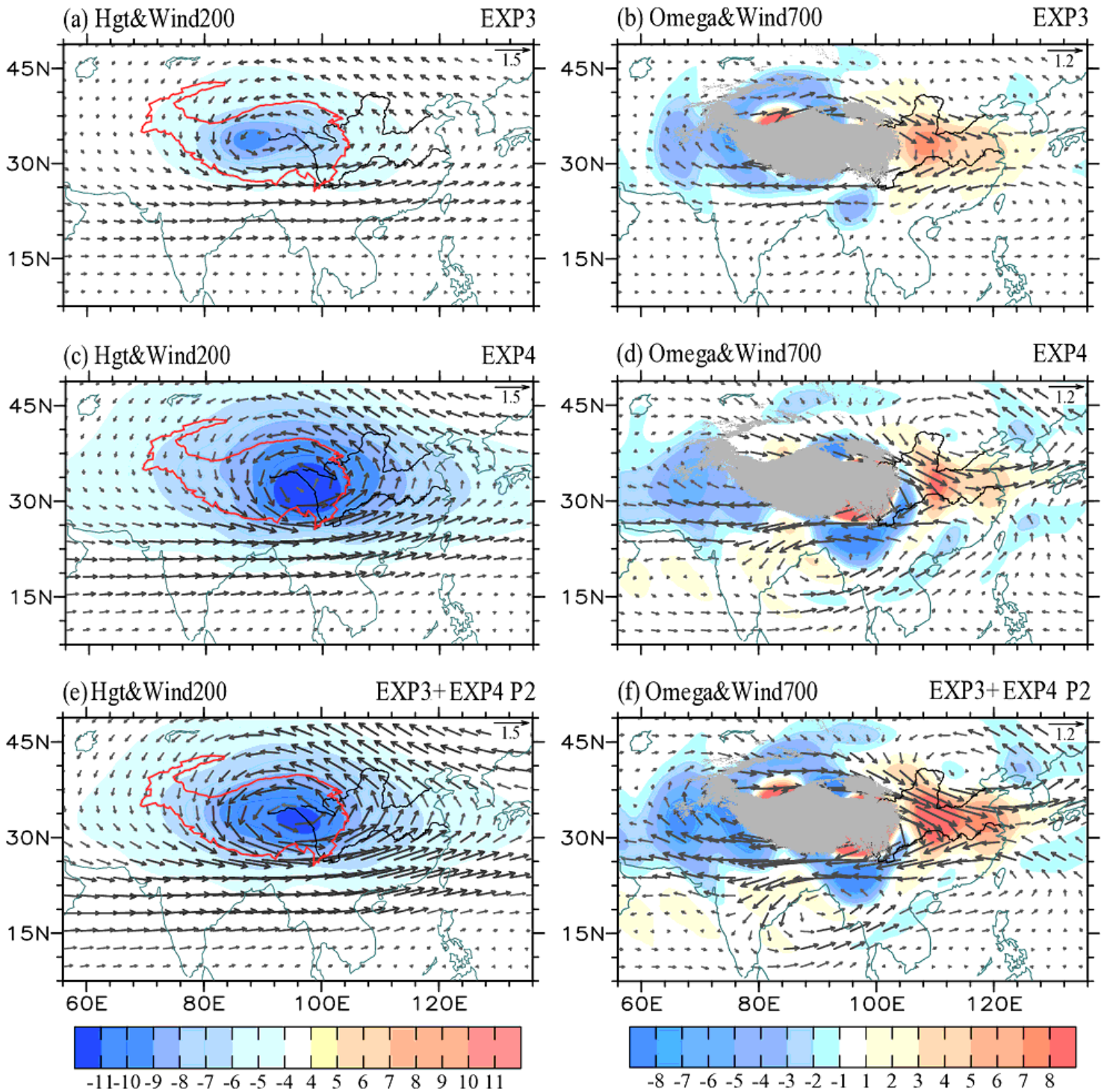
Figure 12

Simulated atmospheric response to the idealized TP forcing added to the climatological spring basic flow for the (a, b) EXP3, (c, d) EXP4, and (e, f) EXP3 + EXP4 during the basic state of P2. The response of (a, c, e) geopotential height (unit: gpm; 1.5×scale in (e)) and wind (vector, m/s) at 200-hPa, and (b, d, f) vertical velocity (unit: 10-3×Pa/s) and wind (vector, m/s) at 700-hPa. The scale for the wind vector is depicted at the top-right flank in each panel.

Supplementary Files

This is a list of supplementary files associated with this preprint. Click to download.

- Supplementarymaterialformanuscriptzhangetal20210619.docx
- OnlineFig.S1.png
- OnlineFig.S2.png
- OnlineFig.S3.png
- OnlineSuppl.4.png